Red phosphorus decorated and doped TiO$_2$ nanofibers for efficient photocatalytic hydrogen evolution from pure water

Yukun Zhu[a,b], Junzhi Li[c], Chung-Li Dong[d], Jun Ren[e], Yu-Cheng Huang[d], Daming Zhao[b], Rongsheng Cai[f], Daixing Wei[b], Xianfeng Yang[g], Chunxiao Lv[a], Wolfgang Theis[f], Yuyu Bu[h], Wei Han[c], Shaohua Shen[b,*], Dongjiang Yang[a,i,**]

[a] State Key Laboratory of Bio-fibers and Eco-textiles, Shandong Collaborative Innovation Center of Marine Biobased Fibers and Ecological Textiles, Institute of Marine Biobased Materials, School of Environmental Science and Engineering, Qingdao University, Qingdao 266071, China
[b] International Research Center for Renewable Energy, State Key Laboratory of Multiphase Flow in Power Engineering, Xi'an Jiaotong University, Xi'an 710049, China
[c] Sino-Russian International Joint Laboratory for Clean Energy and Energy Conversion Technology, College of Physics, Jilin University, Changchun 130012, China
[d] Research Center for X-ray Science, Department of Physics, Tamkang University, Tamsui 25137, Taiwan
[e] School of Chemical and Environmental Engineering, North University of China, Taiyuan 030051, China
[f] Nanoscale Physics Research Laboratory, School of Physics and Astronomy, University of Birmingham, Birmingham, B15 2TT, UK
[g] Analytical and Testing Centre, South China University of Technology, Guangzhou 510640, China
[h] Key Laboratory of Wide Band-Gap Semiconductor Materials and Devices, School of Microelectronics, Xidian University, Xi'an 710071, China
[i] Queensland Micro- and Nanotechnology Centre (QMNC), Griffith University, Nathan Campus, Brisbane, Queensland 4111, Australia

ABSTRACT

In this study, we report a facile strategy to prepare a new class of red phosphorus (RP) decorated and doped TiO$_2$ (A: anatase and B: TiO$_2$(B)) nanofibers with boosted photocatalytic hydrogen evolution reaction (HER) performance from pure water. The optimized TiO$_2$(B)/RP and TiO$_2$(A)/RP heterostructure exhibits significantly enhanced photocatalytic performances, with HER rate reaching 11.4 and 5.3 μmol h^{-1}, respectively. The optical absorption of TiO$_2$ is significantly extended to the visible light region after decoration of RP. And more oxygen vacancies (V$_O$) were introduced by phosphorus doping in the TiO$_2$(B)/RP than TiO$_2$(A)/RP. The theoretical calculations illustrate the formation of V$_O$ can decrease the ratio of effective masses of electron to hole, which gives rise to promoted photoinduced charge separation and transfer. These results suggest that the boosted photocatalytic HER performance should be mainly attributed to the synergetic enhancement in light harvesting and charge separation enabled by RP deposition and P^{5+} doping.

1. Introduction

With increasing interest in hydrogen as an environmentally acceptable, alternative energy carrier with high energy density, several emerging clean-energy technologies have been discovered to pursue sustainable and efficient hydrogen production, such as photocatalytic [1,2], electrocatalytic [3,4] and photoelectrocatalytic [5,6] water splitting into hydrogen. Among them, photocatalytic hydrogen evolution reaction (HER) with semiconductors as photocatalysts has been considered as one of the most important pathways [7], since Fujishima-Honda initially developed TiO$_2$ as a water splitting photocatalyst [8].

To date, TiO$_2$ has been extensively investigated as an ideal model of the photocatalyst [9,10]. Nevertheless, its wide band gap limiting solar light harvesting and the fast charge recombination, as the main drawbacks, have lowered its photocatalytic efficiency to unsatisfied level. To improve the optical absorption properties, many approaches have been devoted to modifying TiO$_2$, including high temperature reduction or hydrogenation [11–13], doping or co-doping with metal and/or nonmetal elements [14–17], and surface sensitization with visible light active semiconductors and dyes [18,19]. Recently, elemental red phosphorus (RP) has emerged as a new class of photocatalyst owing to its narrow bandgap, low cost, nontoxicity, and earth abundance. [20–25] More importantly, its visible-light absorption edge extends up to 700 nm, which is favorable to be as a sensitizer to couple with TiO$_2$ to extend the visible light response. As another determinant for efficient photocatalytic activity, charge separation should be facilitated in TiO$_2$,

with some effective strategies well documented, such as fabrication of heterojunction and phase junction [26–28], surface passivation [29,30], and introduction of oxygen vacancies (V_O) [31,32]. Among them, V_O as a donor source which can bring an increased majority carrier concentration to improve the charge transfer ability. However, the excessive V_O may become the charge recombination centers by trapping the photo-induced electrons [33]. Thus, the density of V_O created in TiO_2 should be optimized to balance their opposite roles as the electron donor and the trap sites.

Given that photocatalytic reactions depend on a sequence of multiple steps, including optical light harvesting, charge separation and transportation, and surface reaction, it is highly desirable to design a coupling strategy that not only can enhance the optical absorption but also can promote the charge transfer in the photocatalysts [34]. In this work, we report a vaporization-deposition strategy to prepare a new class of TiO_2 nanofiber/RP nanolayer core/shell heterostructure with boosted photocatalytic activity for HER from pure water. The optimized $TiO_2(B)/RP$ and $TiO_2(A)/RP$ composites (A: anatase and B: $TiO_2(B)$), displayed significantly enhanced photocatalytic activities than that of bare TiO_2, with the highest HER rates reaching 11.4 and 5.3 $\mu mol\,h^{-1}$, respectively. The great improvement in photocatalytic HER performances could be attributed to the synergy that the introduction of RP nanolayer acting as the visible light sensitizer can enhance light harvesting and the surface phosphorus (P^{5+}) doping induced V_O can facilitate the migration of photogenerated electrons to the photocatalysts surface. This coupling strategy could be applied to the design and fabrication of other highly efficient photocatalysts for solar energy utilization by synergistically improving the light harvesting property and promoting the charge separation ability.

2. Experimental section

2.1. Synthesis of TiO_2/RP heterostructure composites

TiO_2 nanofibers (NFs) were prepared using a hydrothermal method followed by a calcination treatment according to our previous reports [26,27]. Typically, the synthesized $H_2Ti_3O_7$ NFs were calcined in a muffle furnace at 400 °C for 4 h to obtain $TiO_2(B)$ NFs, and calcined at 700 °C for 4 h to produce anatase $TiO_2(A)$ NFs. The commercial red phosphorus (RP, 99.999%, Aladdin) was used after purification as follows: 1 g of RP was added into 60 mL of H_2O, and hydrothermally treated at 200 °C for 12 h in an autoclave to remove the oxide layers.

In a typical process for the synthesis of TiO_2/RP heterostructure composites, 200 mg of TiO_2 NFs and an appropriate amount of RP powder (10 mg~60 mg) were well dispersed in 30 mL of distilled water by ultrasonic treatment for 30 min. The solution was then frozen using liquid nitrogen and freeze-dried to remove water. After that, the obtained pink powder was transferred into a quartz ampoule and sealed by an oxygen-hydrogen flame under a low vacuum condition (-0.09 MPa, high purity Ar filling before pumping) [21,22] The ampoules were heated in a furnace at 500–700 °C (at a ramping rate of 2 °C min^{-1}) for 4 h, then cooled down to 280 °C (at a ramping rate of 1 °C min^{-1}) and held at this temperature for 4 h. After slowly cooled to room temperature at 0.1 °C min^{-1} to prevent the RP vapor transforming into white phosphorus, the as-prepared products were obtained by breaking the capsules and rinsing with CS_2, ethanol and distilled water, respectively. The TiO_2 NFs loaded with different contents (x mg, x = 10–60) of RP were labeled as $TiO_2(B)/RP(x)$ or $TiO_2(A)/RP(x)$.

2.2. Characterization

X-ray diffraction (XRD) was carried out with DX2700 operating at 40 kV and 30 mA equipped with Cu Kα radiation (λ = 1.5418 Å). The morphology and structure of the samples were investigated by an FEI Magellan 400 field emission scanning electron microscope (FESEM) and a JEOL JEM-2100F scanning transmission electron microscope (STEM)

equipped with C_s probe corrector at 200 kV. X-ray photoelectron spectroscopy (XPS) was measured by ESCALAB 250XL electron spectrometer (Thermo Scientific Corporation) with monochromatic 150 W Al Kα radiation. All binding energies were calibrated with C 1s at 284.6 eV. Raman spectra were measured on a LabRAM HR800 evolution with the excitation wavelength of 532 nm. The diffuse reflectance spectra were recorded with Agilent Cary 5000 UV–vis-NIR spectrophotometer using integrated sphere accessory. Electron paramagnetic resonance (EPR) experiments were performed on a Bruker EMX X-band spectrometer and microwave frequency = 9.40 GHz at 100 K in the dark. The synchrotron X-ray absorption spectroscopic (XAS) measurements were conducted at the National Synchrotron Radiation Research Center, Taiwan. The Ti K-edge and P K-edge were carried out at BL17C and BL16A, respectively, and Ti L-edge and O K-edge were performed at BL20A.

2.3. Photocatalytic hydrogen evolution experiments

The photocatalytic hydrogen evolution experiments were carried out in a Pyrex top-irradiation reaction cell at atmospheric pressure. The reactant was pure water, and no sacrificial reagent or pH adjustment was used. 30 mg of the TiO_2/RP sample was dispersed in pure water (150 mL), and H_2PtCl_6 solution equivalent to 3 wt% Pt was added into the reactor. After being purged with argon to remove dissolved air, the solution was irradiated by a 300 W Xe arc lamp (PLS-SXE 300C) with an AM 1.5 G filter to simulate solar light. The power intensity at the central point of reactant was measured to be 500 mW cm^{-2} by PM100D power meter with S302C thermal sensor (Thor Labs) [35]. And the irradiation area was controlled as about 20 cm^2. The temperature of the reactant solution was held at 25 °C by a flow of cooling water. The amount of hydrogen evolution was measured in the air-tight continuous flow system which was connected with the online gas chromatograph (Shimadzu GC-2014C) equipped with a thermal conductivity detector. High purity argon gas (99.999%) was used as a carrier gas.

2.4. Density functional theory calculations

The Vienna Ab-initio Simulation Package (VASP) software on basis of the plane-wave method was utilized for density functional theory (DFT) calculations [36–38]. Our computations employed the generalized gradient approximation (GGA) with Perdew-Burke-Ernzerhof (PBE) exchange-correlation function [39]. The Projector-Augmented-Wave (PAW) method was used to describe the interaction between the ionic core and valence electrons [40]. To localize the Ti 3d states, the well-known Hubbard-like U correction GGA + U method has also been used [41]. U_{eff} = 4.5 eV for $TiO_2(B)$ and U_{eff} = 3.0 eV for $TiO_2(A)$ which are the same as the previous calculations (Table S1) [42]. The threshold for energy convergence was set to 10^{-6} eV. The convergence of the force on each atom was set to 0.02 eV/Å during geometry optimization. The lattice parameters and atomic coordinates were relaxed using the cutoff of 450 eV and Monkhorst-Pack grids of 16 × 16 × 12 for bulk $TiO_2(B)$ and 16 × 16 × 10 k-points for bulk $TiO_2(A)$. The (001) facet of $TiO_2(B)$ and (100) facet of $TiO_2(A)$ were built for comparison. The optimized lattice parameters of $TiO_2(B)$ were a = 12.126 Å, b = 3.739 Å and c = 6.262 Å and those of $TiO_2(A)$ were a = b = 3.789 Å and c = 9.487 Å. In short, the crystal structures, energy band structures and the density of states (DOS) were calculated by the DFT + U method. The effective masses of photogenerated electrons and holes were commutated by the band structures [43,44].

3. Results and discussion

As shown in Fig. 1, the TiO_2/RP core/shell heterostructure composites were fabricated *via* a vaporization-deposition strategy. Firstly, TiO_2 NFs were synthesized by a hydrothermal method and a subsequent calcination treatment. Then, the as-prepared TiO_2 NFs were mixed with
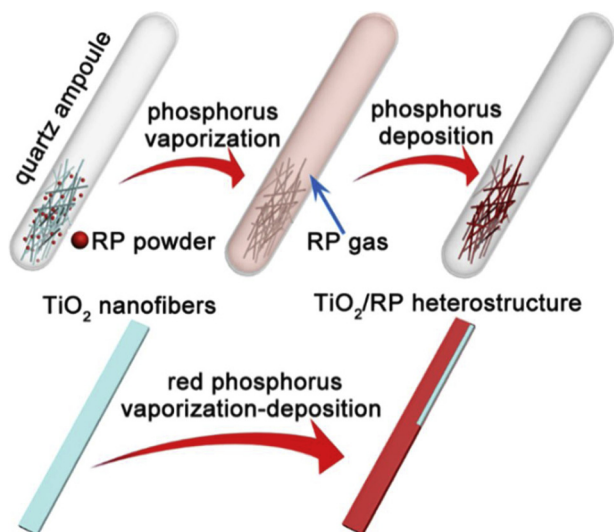
Fig. 1. Schematic illustration for making the TiO_2/RP core/shell heterostructure.

different amounts of RP powders, which were sealed into a quartz ampoule under vacuum condition (Fig. S1). During the calcination process at high temperature (500~700 °C), phosphorus gas was vaporized in the ampoule due to the vacuum environment, and some P element would be doped into the TiO_2 NFs. After that, through a low-temperature procedure, the RP nanolayer would be deposited on the TiO_2 NFs surface with the condensation of phosphorus vapor, to obtain the TiO_2/RP core/shell heterostructure composites [24].

The phase composition and the crystal structure of the TiO_2/RP composites were investigated by X-ray diffraction (XRD). As shown in Fig. S2a, TiO_2(B)/RP(40) composites which were calcined at 500~700 °C were all indexed to TiO_2(B) phase (JCPDS 74-1940). However, in the absence of RP, phase transition from TiO_2(B) to anatase phase (JCPDS 21-1272) started at 550 °C, and the anatase diffraction intensity increased as the temperature was elevated from 500 to 700 °C (Fig. S2b,c). It was thus indicated that the addition of RP can inhibit the phase transformation. With the RP vaporization temperatures optimized to be 600 °C to obtain the TiO_2(B)/RP sample with the highest photocatalytic HER activity (Fig. S3), the TiO_2/RP composites with different RP contents calcined at 600 °C were characterized and discussed in more details in the following sections. As shown in Fig. 2, the

obtained composites exhibited all diffraction peaks indexed to TiO_2(B) (Fig. 2a) or anatase TiO_2 (Fig. 2b). No typical diffraction peaks of RP were observed in the TiO_2/RP composites due to the low amount and poor crystallization of RP. Whereas, when the weight of RP was increased to 80 mg, two small peaks at 2θ = 15.6° and 34.1° corresponding to Hittorf's phosphorus (monoclinic, JCPDS 44-0906) can be observed for TiO_2(A)/RP (Fig. S2d).

Raman spectroscopy was also conducted to verify the structural properties of TiO_2/RP composites. In Fig. S4a, the bands centered at *ca.* 252, 293, 367, 407, 434, 470, 553, and 636 cm^{-1} can be assigned to the typical Raman vibration modes of TiO_2(B), while the bands centered at *ca.* 397, 516, and 637 cm^{-1} can be assigned to the typical Raman vibration modes of TiO_2(A) (Fig. S4b) [27]. For the TiO_2/RP composites, the main peaks centered at 352, 399 and 463 cm^{-1} came from elemental red phosphorus could be observed. Moreover, the intensity of these three peaks increased gradually with the increasing contents of RP added during the vaporization-deposition process. These analysis in XRD and Raman spectra could confirm the successful decoration of RP onto the TiO_2 NFs during the vaporization-deposition process.

The morphologies of as-prepared TiO_2/RP samples were observed by field emission scanning electron microscopy (FESEM) and scanning transmission electron microscopy (STEM). It is clear that all the samples displayed the one-dimensional (1-D) fibril morphology, and the deposition of RP would not bring obvious morphology change (Fig. S5,S6). STEM images (Fig. 3a,d,h,k) further confirm the 1-D fibril structure for all the samples. For the pristine TiO_2 NFs, the lattice fringes which were parallel or vertical to the NFs axis, with interplanar distance of 0.58 nm (Fig. 3b,c) and 0.35 nm (Fig. 3i,j), respectively, could be assigned to the (200) and (101) plane of well crystallized TiO_2(B) and anatase TiO_2, with mesoporous structure clearly observed. After the vaporization-deposition process, a uniform amorphous RP nanolayer was deposited on the surface of TiO_2(B) and TiO_2(A) NFs, with thickness estimated to be 6~7 nm for TiO_2(B)/RP(40) (Fig. 3e,f) and TiO_2(A)/RP(30) (Fig. 3l,m). The corresponding energy dispersive X-ray spectroscopy (EDS) elemental mapping images (Fig. 3g,n) clearly show the uniform distribution of Ti, O, and P elements, confirming the successful deposition of RP nanolayer onto the TiO_2 NFs. It could be further observed that a disordered layer with a thickness of *ca.* 1.5 nm was formed at the interface of TiO_2 NFs and RP nanolayer for both TiO_2(B)/RP and TiO_2(A)/RP, which indicated that defects were introduced into the surface region of TiO_2 NFs during the vaporization-deposition process [11,31].

X-ray photoelectron spectroscopy (XPS) was used to better understand the physicochemical interaction between TiO_2 core and RP shell.
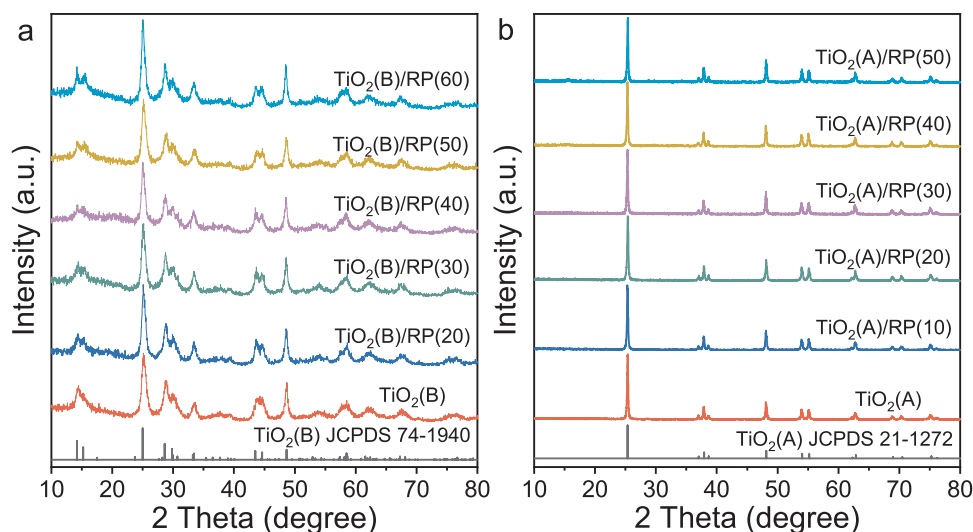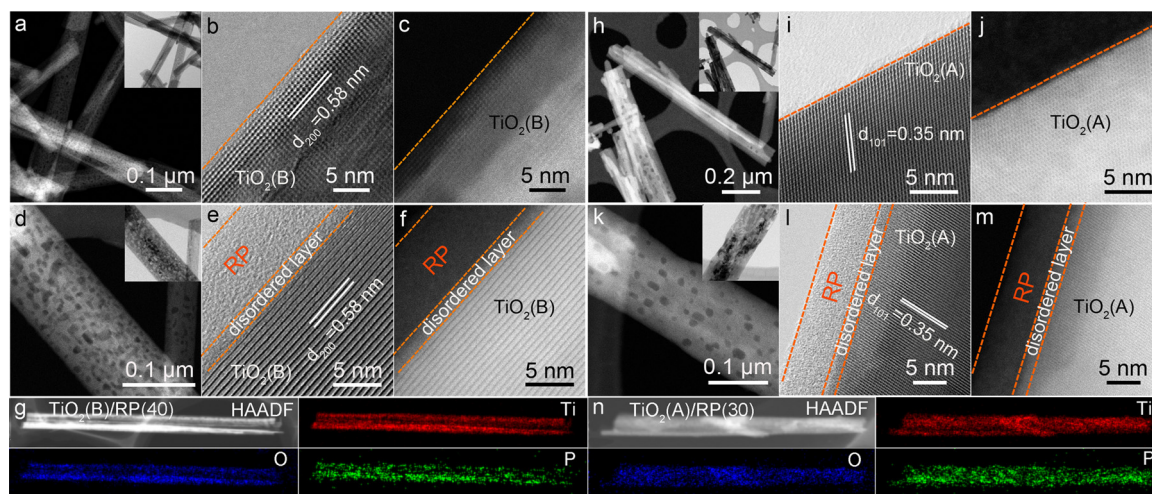

Fig. 2. XRD patterns of TiO_2 and TiO_2/RP composites.

Fig. 3. (a) STEM image, (b,c) aberration corrected bright field (BF) and high-angle annular dark-field (HAADF) STEM images of $TiO_2(B)$, (d) STEM image, (e,f) BF and HAADF STEM images, and (g) HAADF-STEM image and the corresponding EDS mapping of $TiO_2(B)/RP(40)$, (h) STEM image, (i,j) BF and HAADF STEM images of $TiO_2(A)$, (k) STEM image, (l,m) BF and HAADF STEM images, and (n) HAADF-STEM image and the corresponding EDS mapping of $TiO_2(A)/RP(30)$.
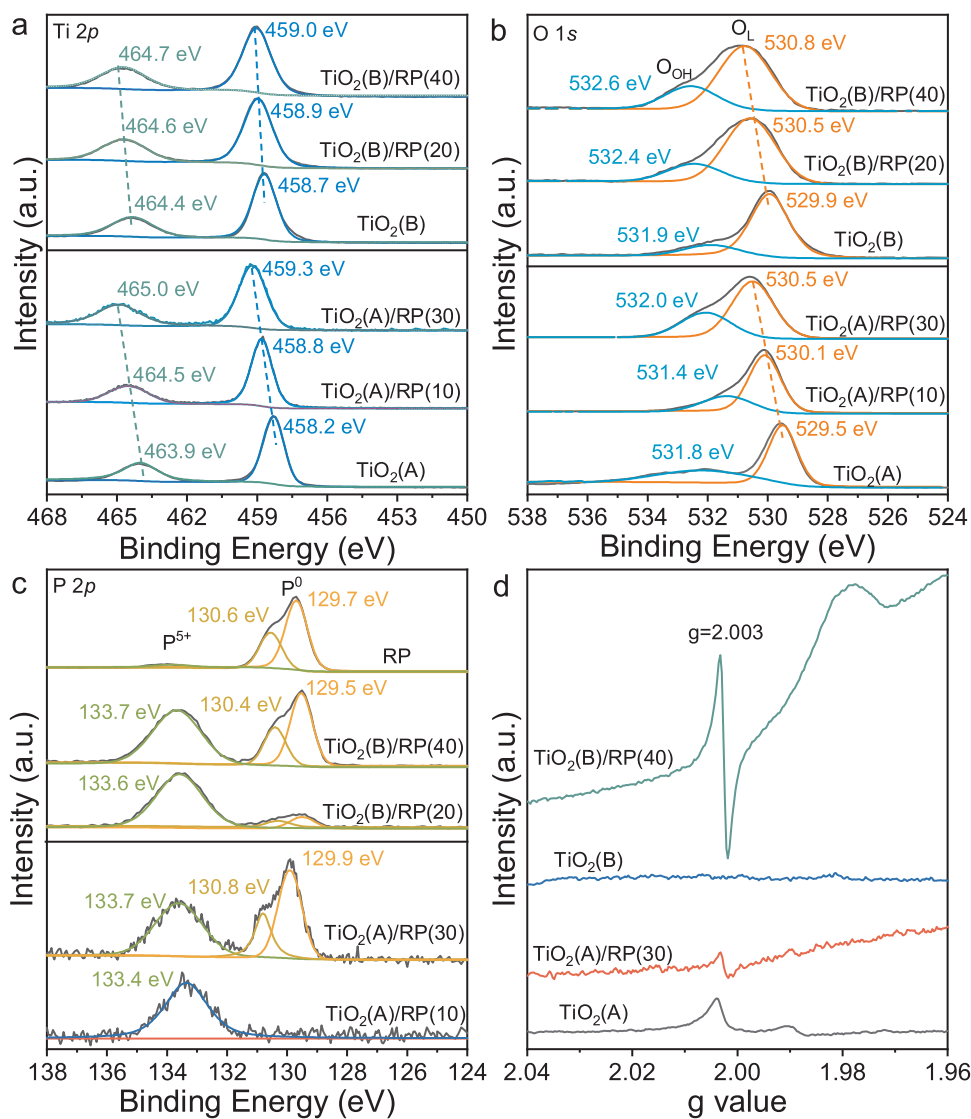

Fig. 4. High resolution XPS spectra of (a) Ti $2p$, (b) O $1s$, (c) P $2p$, and (d) EPR spectra for TiO_2 NFs and TiO_2/RP composites.

The XPS survey spectra revealed the presence of Ti $2p$, O $1s$ and P $2p$ in the TiO_2/RP composites (Fig. S7), indicating that phosphorus has been introduced in the composites successfully. As shown in Fig. 4a, the pristine TiO_2(B) and TiO_2(A) revealed Ti $2p_{3/2}$ peaks at 458.7 eV and 458.2 eV and Ti $2p_{1/2}$ peaks at 464.4 eV and 463.9 eV, respectively, with a spin-orbit splitting of 5.7 eV, indicating the Ti^{4+} chemical state [11]. In comparison, these Ti $2p$ peaks in TiO_2/RP composites were all positively shifted to higher binding energy. As observed in the O $1s$ spectra of the TiO_2(B) and TiO_2(A) (Fig. 4b), the peaks at 529.9 eV and 529.5 eV corresponding to lattice oxygen (O_L) species of TiO_2 were also shifted to higher binding energy for both TiO_2(B)/RP and TiO_2(A)/RP. Moreover, the shift of Ti $2p$ and O $1s$ peaks increased depending on the increasing RP contents in TiO_2/RP composites. These results implied that phosphorus ions were partially doped into TiO_2 during the vaporization-deposition process, and the positive shift in binding energies of Ti $2p$ and O $1s$ should be due to the smaller electronegativity of titanium atoms (1.54) than that of phosphorus atoms (2.19) [45–48]. As shown in Fig. 4b, the O_{OH} peaks of the TiO_2/RP composites exhibited enhanced intensity as compared to the pristine TiO_2 NFs (Table S2). Given the general fact that O_{OH} concentrations correlates to the formation of V_O, TiO_2/RP composites should have more V_O created after the vaporization-deposition process as compared to the pristine TiO_2 NFs [11,31,49]. The P $2p$ spectra of RP show two peaks at 129.7 eV and 130.6 eV (Fig. 4c), which could be attributed to the spin-orbit doublets of P $2p_{3/2}$ and P $2p_{1/2}$, respectively, indicating the P^0 chemical state [20–22]. In comparison to TiO_2(B)/RP(20) and TiO_2(A)/RP(10), TiO_2(B)/RP(40) and TiO_2(A)/RP(30) exhibited increased intensities of P^0 peaks, respectively, demonstrating that the content of elemental RP in the TiO_2/RP composites increased with the increasing contents of RP used in the vaporization-deposition process. Moreover, the peak centered at 133.4 eV~133.7 eV in TiO_2/RP composites suggested the existence of pentavalent oxidation state of P^{5+} that partially substituted some Ti^{4+} in the surface region of TiO_2 NFs with Ti-O-P bonds formed [46,46,47,48,50]. Electron paramagnetic resonance (EPR) spectra were further performed to elucidate the formation of V_O in the surface region of TiO_2 NFs in the TiO_2/RP composites, as induced by the introduction of P^{5+} at Ti^{4+} sites. As shown in Fig. 4d, the TiO_2/RP samples exhibited EPR signals at g = 2.003, suggesting that surface-free electrons were trapped at V_O created in TiO_2 NFs. Further comparison in the intensity of the EPR signals revealed that the concentration of V_O generated in TiO_2(B)/RP was much higher than in TiO_2(A)/RP [11,31]. XPS and EPR results provided clear evidence solidifying the strong chemical interaction between the TiO_2 core and RP shell, which further confirmed the presence of elemental RP and the doping of P^{5+} in the TiO_2/RP core/shell heterostructure.

Fig. 5 shows the optical absorption spectra for the as-prepared samples and their corresponding optical images. As shown in Fig. 5a,b, as compared to the pristine TiO_2 NFs, all the TiO_2/RP composites possessed an extended optical absorption in the visible light region, with the absorption edge gradually red-shifted with the increasing RP amounts added for vaporization-deposition procedure. This should be related to the surface sensitization effect of RP, causing broad and strong visible light absorption in the region of 400~600 nm for both TiO_2(B)/RP and TiO_2(A)/RP composites. Further investigation revealed that TiO_2(B)/RP composites have an additional higher tail-like absorption band in 600~900 nm, as compared to TiO_2(A)/RP, which might be due to the higher concentration of V_O created in TiO_2(B)/RP [12]. Correspondingly, it was obvious that these samples showed a gradient evolution in color from white to brown with the increase of RP contents (Fig. 5c,d), also demonstrating their efficient optical absorption in visible light region. In comparison to the physical mixtures of TiO_2 NFs and RP as the reference, the as-prepared TiO_2/RP composites displayed much stronger optical absorption in the range of 360–600 nm (Fig. S8) with colors deeper and darker (Fig. 5c,d and Fig. S9). These results again evidenced the chemical interaction between TiO_2 and RP in the TiO_2/RP composites with RP shell coated on and P^{5+}/V_O introduced

into TiO_2 NFs by a vaporization-deposition method.

To further evaluate the photocatalytic activity of the obtained composites, photocatalytic HER in pure water without any sacrificial reagents was also performed at ambient pressure and temperature. As shown in Fig. 6a,b and Fig. S10, the pure TiO_2(B) showed no HER performance, while TiO_2(A) and RP exhibited very weak HER activity (0.5 and 2.1 μmol h^{-1}) under simulated solar light illumination (Fig. S11a). Both TiO_2(B)/RP and TiO_2(A)/RP displayed a volcano-type curve of H_2 evolution rates depending on the RP contents, with the highest HER rates reaching 11.4 and 5.3 μmol h^{-1}, respectively, for TiO_2(B)/RP(40) and TiO_2(A)/RP(30) with optimized RP contents. It is noteworthy that the TiO_2(B)/RP(40) composite stands at the highest level of TiO_2-based photocatalysts for hydrogen production *via* pure water splitting (see Table S3). Similar to the trend of photocatalytic HER properties depending on RP contents, the transient photocurrent density was enhanced and Nyquist plots arc radius was decreased after the decoration of RP, which indicate the faster charge carrier transfer and separation in TiO_2/RP composites than that of TiO_2 (Fig. S12) [34]. Based on the analytic discussion on these above characterization results, such drastic improvement in photocatalytic activity can be attributed to the fact that the RP sensitization nanolayer on the TiO_2 NFs could harvest more visible light, and the surface P^{5+} doping induced V_O could enhance charge transportation and inhibit the recombination process. Interestingly, instead of O_2 evolution by water oxidation, hydrogen peroxide (H_2O_2) was produced by photogenerated holes *via* a two-electron process of water oxidation (Fig. S13) [51–53], which would benefit gas separation for hydrogen production *via* pure water splitting. As shown in Fig. 6c, the photocatalytic HER activities were great dependence on the wavelengths under different LEDs light irradiation (Fig. S11b) for both TiO_2(B)/RP(40) and TiO_2(A)/RP(30) composites, confirming that the extended optical absorption by RP decoration was greatly responsive to enhanced HER activities, as compared to the pure TiO_2 NFs. Furthermore, TiO_2/RP composites displayed good photocatalytic stability under a 12 h continuous light irradiation (Fig. 6d). It is interesting that, even though the photocatalytic activity of TiO_2(A) was higher than TiO_2(B), the TiO_2(A)/RP composites showed poor activities than the TiO_2(B)/RP composites. To achieve a better understanding of the intrinsic characters (e.g., the RP sensitization, the introduced P^{5+} dopants and V_O) contributing to the improved photocatalytic activity, X-ray absorption structure spectroscopy (XAS) and density functional theory (DFT) calculations were further performed.

To reveal how these TiO_2/RP composites response to solar light, XAS at Ti L-edge was performed in the dark and under illumination. As shown in Fig. 7a, the intensity of Ti L-edge obtained under the illuminated condition was slightly lessened in comparison with that in the dark, suggesting the electronic structure was changed upon light illumination. Moreover, TiO_2/RP displayed a more significant decrease in the intensity than TiO_2 NFs, indicating that TiO_2/RP composites were more sensitive to light. Notably, the spectral difference (marked by dashed squares) between dark and illumination was more remarkable for TiO_2(B)/RP(40) than TiO_2(A)/RP(30), revealing more efficient electron excitation to the unoccupied Ti 3d states in the conduction band of TiO_2(B)/RP(40). These results implied that RP could benefit electron photoexcitation and contribute to the increased photocatalytic activity of TiO_2/RP composites. One may also note that the spectral profiles of TiO_2 NFs were quite different from those of TiO_2/RP, suggesting that RP could modify the electronic and atomic structures of TiO_2 NFs. Therefore, XAS at Ti K-edge was also investigated and displayed in Fig. 7b. According to similar features indicated by vertical dashed lines as well as the features presented in the pre-peak region (marked by dashed squares), it is suggested the decoration of RP does not affect severely the crystal structure of TiO_2 NFs (either TiO_2(B) or TiO_2(A)), which is in agreement with the XRD characterization (Fig. 2) [54]. Anyhow, further investigation on the pre-peak region (about 4969–4977 eV) mainly originated from Ti 3d states would be of
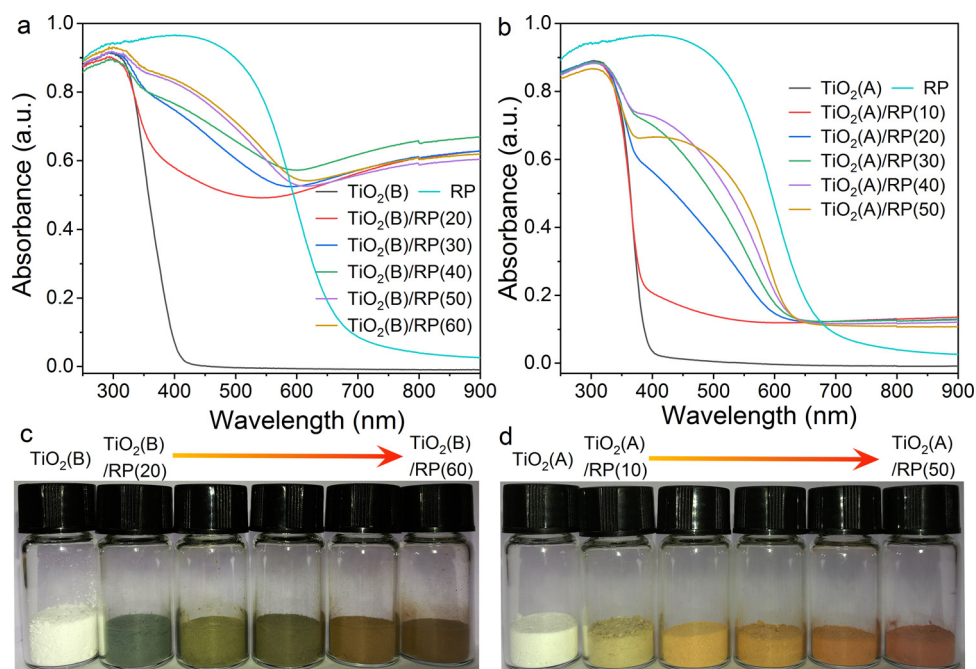
Fig. 5. (a, b) Optical absorption spectra and (c, d) the corresponding optical images of TiO_2 and TiO_2/RP composites.
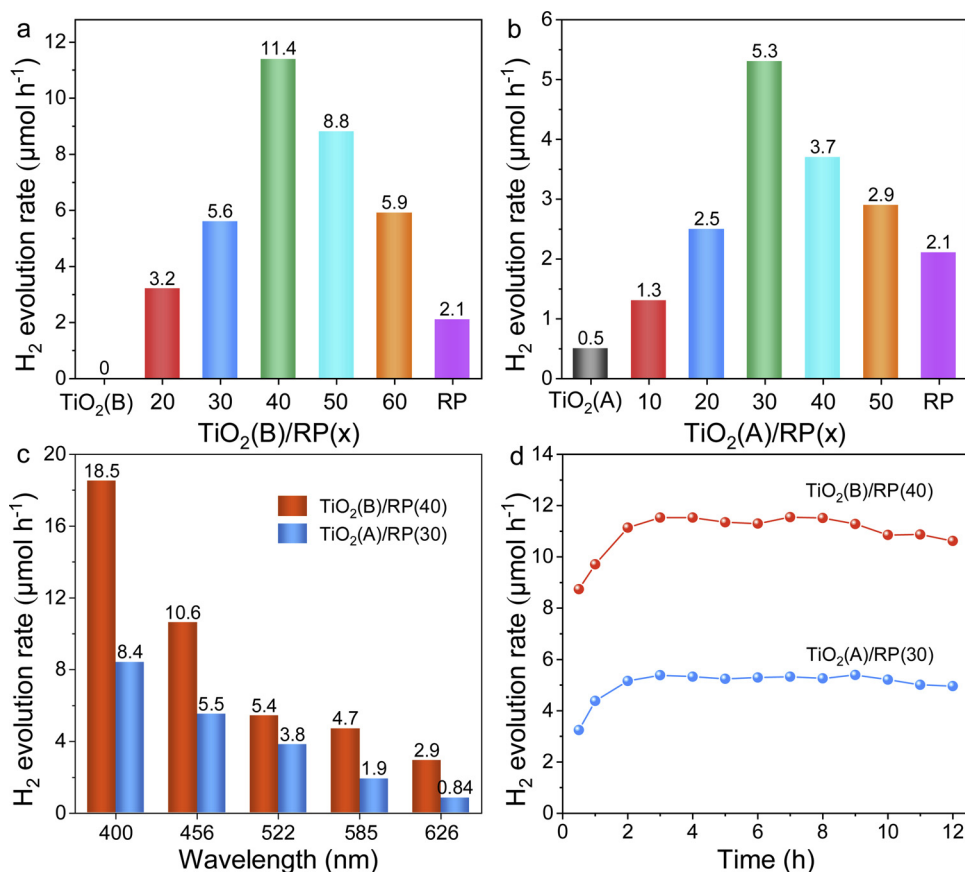

Fig. 6. Photocatalytic HER from pure water activities of (a) $TiO_2(B)/RP$ and (b) $TiO_2(A)/RP$ composites under simulated solar light irradiation, (c) Wavelength-dependent photocatalytic HER rates $TiO_2(B)/RP(40)$ and $TiO_2(A)/RP(30)$ under different LEDs light irradiation with center wavelength of 400 nm, 456 nm, 522 nm, 585 nm, and 626 nm, respectively, (d) Time-course of photocatalytic HER rates over $TiO_2(B)/RP(40)$ and $TiO_2(A)/RP(30)$ under simulated solar light irradiation.

importance to look into the fine structures. After background subtraction, the pre-peak area was shown in Fig. 7c and decomposed into four components, A_1, A_2, A_3, and A_4 [55]. As RP was decorated onto TiO_2 NFs, the peak A_2 of TiO_2/RP was greater than that of bare TiO_2 NFs, indicating that P^{5+} doping induced the formation of V_O in TiO_2 NFs and thus increased the five-fold coordinated geometry or disordered local

atomic structure. A more significant increase in peak A_2 intensity was observed in $TiO_2(B)/RP(40)$ in comparison with $TiO_2(A)/RP(30)$, meaning that more V_O was created in $TiO_2(B)/RP(40)$, agreeing well with optical absorption spectra as well as EPR spectra. To further verify the induction of V_O in TiO_2 NFs by P^{5+} doping, the Fourier-transform of extend X-ray absorption fine structures (EXAFS) $k^3\chi$ data at Ti K-edge
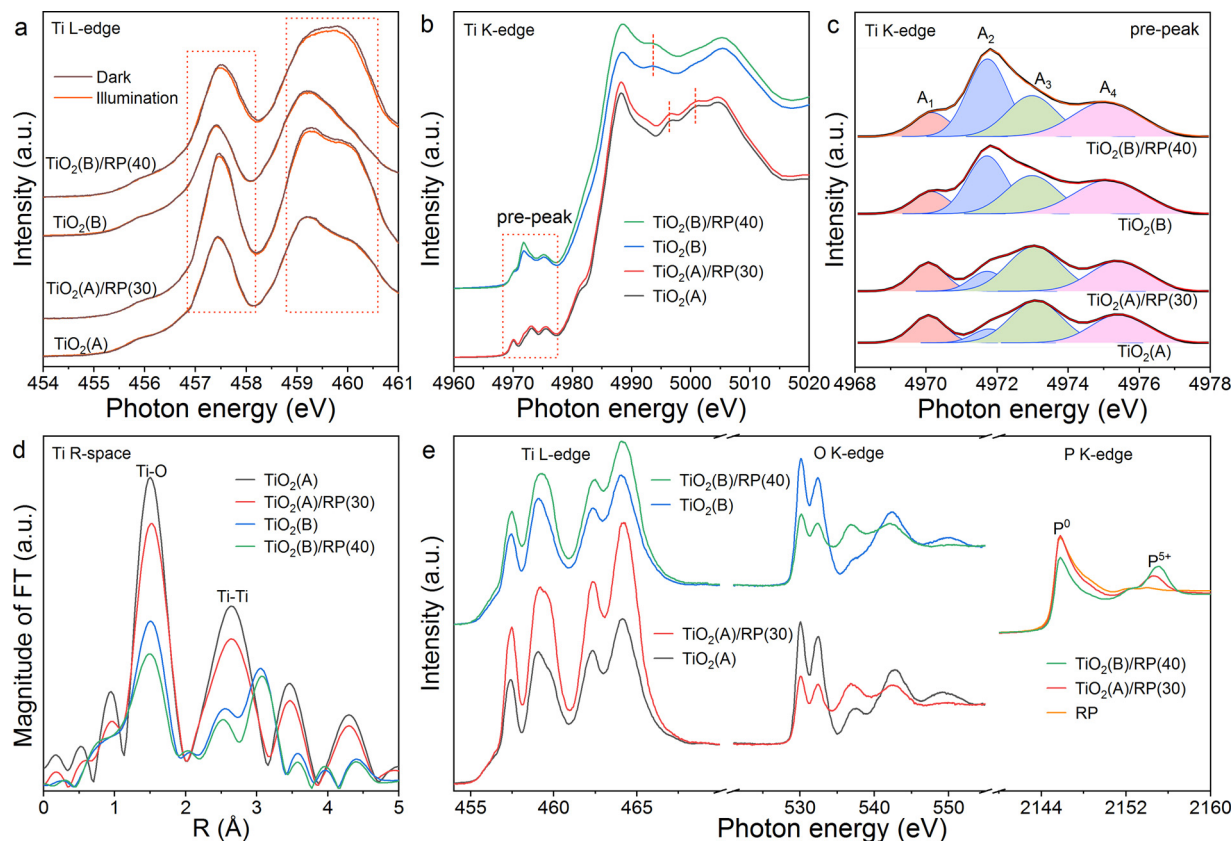
Fig. 7. (a) The XAS spectra at Ti L-edge performed in the dark and under illumination, (b) Ti K-edge XAS spectra, (c) the pre-peak area of Ti K-edge XAS spectra, (d) the Fourier-transform of the EXAFS $k^3\chi$ data at Ti K-edge and (e) the XAS spectra at Ti L-edge, O K-edge and P K-edge of RP, TiO_2 and TiO_2/RP composites.

was also investigated (Fig. 7d). The predominant peak at about 1.5 Å was attributable to the first shell Ti-O bonds, and the greater amplitude of TiO_2 than that of TiO_2/RP suggested that RP tended to induce V_O in the TiO_2/RP composites, especially for TiO_2(B)/RP(40) [54,56]. Analytical results above elucidated that RP created V_O in TiO_2 NFs and thus affected the local atomic structures. The presence of V_O in TiO_2 NFs gives rise to two electrons remain behind, and these electrons tend to move toward neighbor Ti site owing to the maintenance of charge balance. To further elucidate the effect of RP on the electronic structure, XAS at Ti L-edge, O K-edge, and P K-edge are displayed in Fig. 7e. For Ti L-edge, the peak intensities of TiO_2/RP were greater than that of TiO_2, implying that Ti lost some charges in the presence of RP [55]. Whereas the change in peak intensities of O K-edge exhibited the opposite trend to Ti L-edge, which suggested that charges should be transferred from Ti to O [55,57], as RP was introduced. Notably, Ti lost more charges in TiO_2(A)/RP than in TiO_2(B)/RP, while electron density around O site for TiO_2(B)/RP was higher. Considering the electronegativity of Ti (1.54), O (3.44), and P (2.19), oxygen has the highest ability to attract the electrons, and therefore electrons at P site may migrate to O site. The P K-edge had two main features associated with P^0 and P^{5+} states [58,59]. It is clear that RP exhibited mostly the P^0 states. However, when RP was decorated onto TiO_2 NFs, the P^{5+} states increased. TiO_2(B)/RP(40) presented even more P^{5+} states than TiO_2(A)/RP(30), which indicated that there were more P−O bonds in TiO_2(B)/RP(40). Consequently, the high electron density around the O site in TiO_2(B)/RP could be contributable to more P−O bonds formed. The presence of RP not only created V_O by P^{5+} doping but also redistributed the electrons from P to O sites. Notably, the O $2p$ states dominated the valence band maximum, and thus the high electron density at O sites in TiO_2(B)/RP resulted in the high possibility for electrons on the O $2p$ valence band to be excited to the Ti $3d$ conduction band under solar irradiation, which has been already verified by the

solar light-dependent XAS revealed in Fig. 7a.

DFT calculations were further performed to reveal the contribution of V_O to the efficient charge transfer process and the improved photocatalytic activity, by elucidating the electronic structure and effective carrier masses. According to the TEM experimental investigation, the (001) and (100) planes were the predominantly exposed crystal facets for TiO_2(B) and TiO_2(A) [26], respectively, which were then built for the comparative DFT calculations. Fig. 8a,b show the schematics of the P^{5+} doping induced V_O in TiO_2(B) and TiO_2(A) supercells, with one P^{5+} dopant replacing one Ti atom which induced one V_O. The P^{5+} doping reduced the V_O formation energy by 1.60 eV for TiO_2(A) and 1.05 eV for TiO_2(B) (see calculation details in Supporting information), which further indicated that the P-induced formation of V_O in TiO_2(B) was more favorable than in TiO_2(A). As shown in Fig. 8c, in comparison to the total density of states (TDOS) of pristine TiO_2, impurity states created by V_O can be seen in P-doped TiO_2, which were responsible for the observed tale-like absorption in Fig. 5. The effective masses of electrons and holes can be used to assess the transfer rate of charge carriers. It has been well accepted that a lower charge carrier effective mass corresponds to a higher charge carrier mobility, and the large difference between effective masses of electron and hole suggests a low recombination rate of the electron-hole pairs [43,44]. Therefore, the relative effective masses of holes and electrons in pristine and P-doped TiO_2 NFs were further computed, by the quadratic fits of the band structures, to examine how the P doping induced V_O affected the mobility and separation of charge carriers. The carrier effective masses (m*) were calculated and shown in Table S4. The value of the effective mass of electrons (m_e*) was smaller than that of the corresponding value of holes (m_h*) for each sample and thus electron had higher mobility than hole in TiO_2. The values of m_e*/m_h* were then determined to be 0.918, 0.544, 0.894 and 0.612 for TiO_2(B), P doped TiO_2(B), TiO_2(A) and P doped TiO_2(A), respectively. It is clear that the
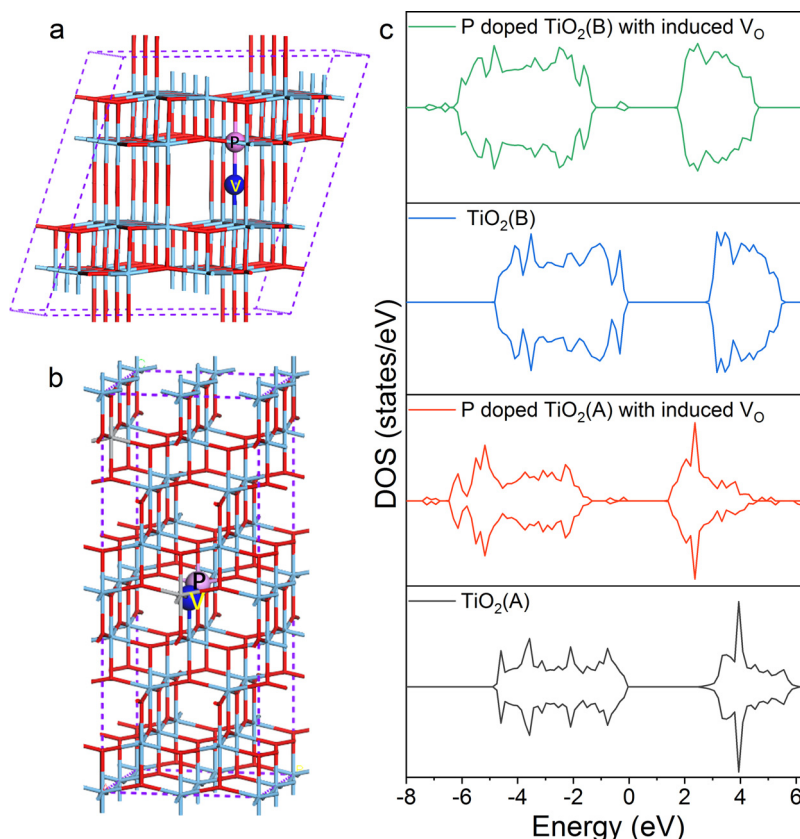
Fig. 8. Schematic of the P^{5+} doped induced V_O in (a) $TiO_2(B)$ and (b) $TiO_2(A)$ supercell. (c) The total density of states (TDOS) for pristine and P-doped induced V_O in TiO_2.

P^{5+} doping induced V_O can decrease the ratio of electron to hole effective mass (m_e*/m_h*) significantly, indicating the reduced recombination rates of the charge carriers in P doped TiO_2 NFs. Moreover, in comparison to P doped $TiO_2(A)$, P doped $TiO_2(B)$ possessed the smaller m_e*/m_h*, implying the more efficient charge carrier separation. These DFT calculations revealed that the formation of V_O was easier in $TiO_2(B)$ by P^{5+} doping than in $TiO_2(A)$, as experimentally supported by the EPR and XAS results indicating that more V_O was generated in $TiO_2(B)/RP$ than $TiO_2(A)/RP$. Thus, the $TiO_2(B)/RP$ composites with more V_O introduced would have more effective charge separation, which could contribute to the great improvement in photocatalytic activity for hydrogen evolution under solar light, together with the excellent visible light absorption of the deposited RP nanolayer as the photosensitizer.

Based on the above experimental and theoretical results, the photocatalytic H_2 production mechanism was proposed in Fig. 9. Coating RP sensitization nanolayer on the TiO_2 NFs surface can enhance optical absorption in the visible light region, and the doping of P^{5+} in TiO_2 crystal lattices would introduce V_O in the surface region of TiO_2 NFs

and thus facilitate the charge transfer process. Thus, more electrons can be photoexcited and then efficiently transferred to the photocatalyst surface active sites, which synergistically boosts photocatalysis efficiency of the TiO_2/RP composites.

4. Conclusion

In summary, a novel vaporization-deposition strategy was developed to simultaneously coat red phosphorous (RP) on and dope P^{5+} into the surface of TiO_2 nanofibers. It was demonstrated that the obtained TiO_2/RP composites showed much increased photocatalytic activity for hydrogen production from pure water. By optimizing the RP amounts used during the vaporization-deposition process, the TiO_2/RP composites showed photocatalytic hydrogen evolution rates as high as 11.4 and 5.3 $\mu mol\,h^{-1}$, with TiO_2 existing in $TiO_2(B)$ and anatase phase, respectively, under simulated solar illumination. Experimental and theoretical investigation evidenced that coating light sensitive RP nanolayer on the TiO_2 surface can enhance optical absorption in the visible light region, and the doping of P^{5+} in TiO_2 crystal lattice would introduce V_O in the TiO_2 surface region and thus facilitate charge transfer. Thus, more electrons can be photoexcited and then efficiently transferred to the photocatalyst surface active sites, which synergistically boosted photocatalysis efficiency of the TiO_2/RP composites. This study presented an alternative strategy to design novel composite photocatalysts with efficient photocatalytic performances by synergistically extending optical absorption and improving charge carrier separation.
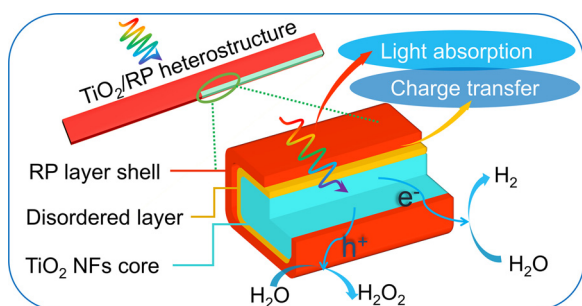
Fig. 9. Illustration of the charge transfer processes in TiO_2/RP composites.

Appendix A. Supplementary data

Supplementary material related to this article can be found, in the online version, at doi:https://doi.org/10.1016/j.apcatb.2019.117764.

References

[1] A. Kudo, Y. Miseki, Heterogeneous photocatalyst materials for water splitting, Chem. Soc. Rev. 38 (2009) 253–278.

[2] X. Chen, S. Shen, L. Guo, S.S. Mao, Semiconductor-based photocatalytic hydrogen generation, Chem. Rev. 110 (2010) 6503–6570.

[3] Y. Zheng, Y. Jiao, M. Jaroniec, S. Qiao, Advancing the electrochemistry of the hydrogen evolution reaction through combining experiment and theory, Angew. Chem. Int. Ed. 54 (2015) 52–65.

[4] X. Zou, Y. Zhang, Noble metal-free hydrogen evolution catalysts for water splitting, Chem. Soc. Rev. 44 (2015) 5148–5180.

[5] I. Roger, M.A. Shipman, M.D. Symes, Earth-abundant catalysts for electrochemical and photoelectrochemical water splitting, Nat. Rev. Chem. 1 (2017) 0003.

[6] K. Sivula, R. Van De Krol, Semiconducting materials for photoelectrochemical energy conversion, Nat. Rev. Mater. 1 (2016) 15010.

[7] S. Chen, T. Takata, K. Domen, Particulate photocatalysts for overall water splitting, Nat. Rev. Mater. 2 (2017) 17050.

[8] A. Fujishima, K. Honda, Electrochemical photolysis of water at a semiconductor electrode, Nature 238 (1972) 37–38.

[9] Y. Ma, X. Wang, Y. Jia, X. Chen, H. Han, C. Li, Titanium dioxide-based nanomaterials for photocatalytic fuel generations, Chem. Rev. 114 (2014) 9987–10043.

[10] J. Schneider, M. Matsuoka, M. Takeuchi, J. Zhang, Y. Horiuchi, M. Anpo, D.W. Bahnemann, Understanding TiO$_2$ photocatalysis: mechanisms and materials, Chem. Rev. 114 (2014) 9919–9986.

[11] J. Cai, M. Wu, Y. Wang, H. Zhang, M. Meng, Y. Tian, X. Li, J. Zhang, L. Zheng, J. Gong, Synergetic enhancement of light harvesting and charge separation over surface-disorder engineered TiO2 photonic crystals, Chem 2 (2017) 877–892.

[12] Y. Liu, L. Tian, X. Tan, X. Li, X. Chen, Synthesis, properties, and applications of black titanium dioxide nanomaterials, Sci. Bull. (Beijing) 62 (2017) 431–441.

[13] Y. Yang, L. Yin, Y. Gong, P. Niu, J. Wang, L. Gu, X. Chen, G. Liu, L. Wang, H. Cheng, An unusual strong visible-light absorption band in red anatase TiO$_2$ photocatalyst induced by atomic hydrogen-occupied oxygen vacancies, Adv. Mater. 30 (2018) 1704479.

[14] V. Kumaravel, S. Mathew, J. Bartlett, S.C. Pillai, Photocatalytic hydrogen production using metal doped TiO$_2$: a review of recent advances, Appl. Catal. B 244 (2019) 1021–1064.

[15] H. Lin, C.Y. Shih, Efficient one-pot microwave-assisted hydrothermal synthesis of m (M = Cr, Ni, Cu, Nb) and nitrogen Co-doped TiO$_2$ for hydrogen production by photocatalytic water splitting, J. Mol. Catal. A Chem. 411 (2016) 128–137.

[16] X. Hong, J. Tan, H. Zhu, N. Feng, Y. Yang, J.T.S. Irvine, L. Wang, G. Liu, H. Cheng, Control of spatially homogeneous distribution of heteroatoms to produce red TiO$_2$ photocatalyst for visible-light photocatalytic water splitting, Chem. Eur. J. 25 (2019) 1787–1794.

[17] R. Marschall, L. Wang, Non-metal doping of transition metal oxides for visible-light photocatalysis, Catal. Today 225 (2014) 111–135.

[18] F. Xu, J. Zhang, B. Zhu, J. Yu, J. Xu, CuInS$_2$ sensitized TiO$_2$ hybrid nanofibers for improved photocatalytic CO$_2$ reduction, Appl. Catal. B 230 (2018) 194–202.

[19] A. Tiwari, N.V. Krishna, L. Giribabu, U. Pal, Hierarchical porous TiO$_2$ embedded unsymmetrical zinc–Phthalocyanine sensitizer for visible-light-Induced photocatalytic H$_2$ production, J. Phys. Chem. C 122 (2018) 495–502.

[20] F. Wang, W.K.H. Ng, J.C. Yu, H. Zhu, C. Li, L. Zhang, Z. Liu, Q. Li, Red phosphorus: an elemental photocatalyst for hydrogen formation from water, Appl. Catal. B 111–112 (2012) 409–414.

[21] Z. Shen, Z. Hu, W. Wang, S.F. Lee, D.K.L. Chan, Y. Li, T. Gua, J.C. Yu, Crystalline phosphorus fibers: controllable synthesis and visible-light-Driven photocatalytic activity, Nanoscale 6 (2014) 14163–14167.

[22] Z. Hu, L. Yuan, Z. Liu, Z. Shen, J.C. Yu, An elemental phosphorus photocatalyst with a record high hydrogen evolution efficiency, Angew. Chem. Int. Ed. 55 (2016) 1–7.

[23] W. Li, Y. Zhang, G. Tian, S. Xie, Q. Xu, L. Wang, J. Tian, Y. Bu, Fabrication of graphene-modified nano-sized red phosphorus for enhanced photocatalytic performance, J. Mol. Catal. A Chem. 423 (2016) 356–364.

[24] L. Jing, R. Zhu, D.L. Phillips, Y.C. Yu, Effective prevention of charge trapping in graphitic carbon nitride with nanosized red phosphorus modifcation for superior photo(electro)catalysis, Adv. Funct. Mater. (2017) 1703484.

[25] J. Wang, D. Zhang, J. Deng, S. Chen, Fabrication of phosphorus Nanostructures/ TiO$_2$ composite photocatalyst with enhancing photodegradation and hydrogen production from water under visible light, J. Colloid Interface Sci. 516 (2018) 215–223.

[26] L. Zhang, D. Jing, X. She, H. Liu, D. Yang, Y. Lu, J. Li, Z. Zheng, L. Guo, Heterojunctions in g-C$_3$N$_4$/TiO$_2$(B) nanofibres with exposed (001) plane and enhanced visible-light photoactivity, J. Mater. Chem. A Mater. Energy Sustain. 2 (2014) 2071–2078.

[27] D. Yang, H. Liu, Z. Zheng, Y. Yuan, J. Zhao, E.R. Waclawik, X. Ke, H. Zhu, An

[28] efficient photocatalyst structure: TiO$_2$(B) nanofibers with a shell of anatase nanocrystals, J. Am. Chem. Soc. 131 (2009) 17885–17893.

[28] J. Zhang, Q. Xu, Z. Feng, M. Li, C. Li, Importance of the relationship between surface phases and photocatalytic activity of TiO$_2$, Angew. Chem. Int. Ed. 47 (2008) 1766–1769.

[29] L. Gao, Y. Li, J. Ren, S. Wang, R. Wang, G. Fu, Y. Hu, Passivation of defect states in anatase TiO$_2$ hollow spheres with Mg doping: realizing efficient photocatalytic overall water splitting, Appl. Catal. B 202 (2017) 127–133.

[30] Y. Pu, Y. Ling, K. Chang, C. Liu, J. Zhang, Y. Hsu, Y. Li, Surface passivation of TiO$_2$ nanowires using a facile precursor treatment approach for photoelectrochemical water oxidation, J. Phys. Chem. C 118 (2014) 15086–15094.

[31] Y. Liu, Y. Li, S. Yang, Y. Lin, J. Zuo, H. Liang, F. Peng, Revealing the relationship between photocatalytic properties and structure characteristics of TiO$_2$ reduced by hydrogen and carbon monoxide treatment, ChemSusChem 11 (2018) 2766–2775.

[32] G. Wang, H. Wang, Y. Ling, Y. Tang, X. Yang, R.C. Fitzmorris, C. Wang, J. Zhang, Y. Li, Hydrogen-treated TiO$_2$ nanowire arrays for photoelectrochemical water splitting, Nano Lett. 11 (2011) 3026–3033.

[33] J.H. Kim, Y.J. Jang, J.H. Kim, J.W. Jang, S.H. Choi, J.S. Lee, Defective ZnFe$_2$O$_4$ nanorods with oxygen vacancy for photoelectrochemical water splitting, Nanoscale 7 (2015) 19144–19151.

[34] Y. Zhu, J. Ren, X. Yang, G. Chang, Y. Bu, G. Wei, W. Han, D. Yang, Interface engineering of 3D BiVO$_4$/Fe-based layered double hydroxide core/shell nanostructures for boosting photoelectrochemical water oxidation, J. Mater. Chem. A 5 (2017) 9952–9959.

[35] F. Quan, J. Zhang, D. Li, Y. Zhu, Y. Wang, Y. Bu, Y. Qin, Y. Xia, S. Komarneni, D. Yang, Biomass as a template leads to CdS@Carbon aerogels for efficient photocatalytic hydrogen evolution and stable photoelectrochemical cells, ACS Sustain. Chem. Eng. 6 (2018) 14911–14918.

[36] G. Kresse, J. Furthmüller, Efficient iterative schemes for ab initio total-energy calculations using a plane-wave basis set, Phys. Rev. B 54 (1996) 11169–11186.

[37] G. Kresse, J. Furthmüller, Efficiency of ab-initio total energy calculations for metals and semiconductors using a plane-wave basis set, Comput. Mater. Sci. 6 (1996) 15–50.

[38] G. Chang, J. Ren, X. She, K. Wang, S. Komarneni, D. Yang, How heteroatoms (Ge, N, P) improve the electrocatalytic performance of graphene: theory and experiment, Sci. Bull. (Beijing) 63 (2018) 155–158.

[39] J.P. Perdew, K. Burke, M. Ernzerhof, Generalized gradient approximation made simple, Phys. Rev. Lett. 77 (1996) 3865–3868.

[40] G. Kresse, D. Joubert, From ultrasoft pseudopotentials to the projector augmented-wave method, Phys. Rev. B 59 (1999) 1758–1775.

[41] V.I. Anisimov, J. Zaanen, O.K. Andersen, Band theory and mott insulators: hubbard U instead of stoner I, Phys. Rev. B 44 (1991) 943–954.

[42] M. Nolan, S.D. Elliott, J.S. Mulley, R.A. Bennett, M. Basham, P. Mulheran, Electronic structure of point defects in controlled self-doping of the TiO$_2$ (110) surface: combined photoemission spectroscopy and density functional theory study, Phys. Rev. B 77 (2008) 235424.

[43] P. Liao, E.A. Carter, New concepts and modeling strategies to design and evaluate photo-electro-catalysts based on transition metal oxides, Chem. Soc. Rev. 42 (2013) 2401–2422.

[44] J. Yu, P. Zhou, Q. Li, New insight into the enhanced visible-light photocatalytic activities of B-, C- and B/C-Doped anatase TiO$_2$ by first-principles, Phys. Chem. Chem. Phys. 15 (2013) 12040–12047.

[45] S.Y. Mendiola-Alvarez, M.A. Hernández-Ramírez, J.L. Guzmán-Mar, L.L. Garza-Tovar, L. Hinojosa-Reyes, Phosphorous-doped TiO$_2$ nanoparticles: synthesis, characterization, and visible photocatalytic evaluation on sulfamethazine degradation, Environ. Sci. Pollut. Res. 26 (2019) 4180–4191.

[46] K. Wang, K. Yu, L. Liu, L. Hou, F. Jin, Hierarchical P-doped TiO$_2$ nanotubes Array@Ti plate: towards advanced CO$_2$ photocatalytic reduction catalysts, Ceram. Int. 42 (2016) 16405–16411.

[47] D. Qin, Q. Wang, J. Chen, C. He, Y. Li, C. Wang, J. Quan, C. Tao, X. Lu, Phosphorus-doped TiO$_2$ nanotube arrays for visible-light-driven photoelectrochemical water oxidation, Sustain. Energy Fuels 1 (2017) 248–253.

[48] R. Zheng, L. Lin, J. Xie, Y. Zhu, Y. Xie, State of doped phosphorus and its influence on the physicochemical and photocatalytic properties of P-Doped titania, J. Phys. Chem. C 112 (2008) 15502–15509.

[49] Z. Wang, X. Mao, P. Chen, M. Xiao, S.A. Monny, S. Wang, M. Konarova, A. Du, L. Wang, Understanding the roles of oxygen vacancies in hematite-based photoelectrochemical processes, Angew. Chem. Int. Ed. 58 (2019) 1030–1034.

[50] C. Sotelo-Vazquez, N. Noor, A. Kafizas, R. Quesada-Cabrera, D.O. Scanlon, A. Taylor, J.R. Durrant, I.P. Parkin, Multifunctional P-Doped TiO$_2$ films: a new approach to self-cleaning, transparent conducting oxide materials, Chem. Mater. 27 (2015) 3234–3242.

[51] W. Wang, G. Li, T. An, D.K.L. Chan, J.C. Yu, P.K. Wong, Photocatalytic hydrogen evolution and bacterial inactivation uilizing sonochemical-synthesized g-C$_3$N$_4$/red phosphorus hybrid nanosheets as a wide-spectral-responsive photocatalyst: the role of type I band alignment, Appl. Catal. B 238 (2018) 126–13.

[52] L. Wang, S. Cao, K. Guo, Z. Wu, Z. Ma, L. Piao, Simultaneous hydrogen and peroxide production by photocatalytic water splitting, Chin. J. Catal. 40 (2019) 470–475.

[53] S. Siahrostami, G.L. Li, V. Viswanathan, J.K. Nørskov, One- or two-electron water oxidation, hydroxyl radical, or H$_2$O$_2$ evolution, J. Phys. Chem. Lett. 8 (2017) 1157–1160.

[54] W. Zhou, J. Liu, J. Song, J. Li, J. Liu, X. Huang, Surface-electronic-state-modulated, single-crystalline (001) TiO$_2$ nanosheets for sensitive electrochemical sensing of heavy-metal ions, Anal. Chem. 89 (2017) 3386–3394.

[55] S.J. Stewart, M. Fernández-García, C. Belver, B.S. Mun, F.G. Requejo, Influence of N-doping on the structure and electronic properties of titania nanoparticle

photocatalysts, J. Phys. Chem. B 110 (2006) 16482–16486.

[56] I. Krivtsov, M. Ilkaeva, E. Salas-Colera, Z. Amghouz, J.R. García, E. Díaz, S. Ordóñez, S. Villar-Rodil, Consequences of nitrogen doping and oxygen enrichment on titanium local order and photocatalytic performance of TiO_2 anatase, J. Phys. Chem. C 121 (2017) 6770–6780.

[57] O. Trejo, K.E. Roelofs, S.C. Xu, M. Logar, R. Sarangi, D. Nordlund, A.L. Dadlani, R. Kravec, N.P. Dasgupta, S.F. Bent, F.B. Prinz, Quantifying geometric strain at the PbS QD-TiO_2 anode interface and its effect on electronic structures, Nano Lett. 15 (2015) 7829–7836.

[58] W. Lei, Y. Mi, R. Feng, P. Liu, S. Hu, J. Yu, X. Liu, J.A. Rodriguez, J. Wang, L. Zheng, K. Tang, S. Zhu, G. Liu, M. Liu, Hybrid 0D–2D black phosphorus quantum dots--graphitic carbon nitride nanosheets for efficient hydrogen evolution, Nano Energy 50 (2018) 552–561.

[59] M. Yoshida, T. Mineo, Y. Mitsutomi, F. Yamamoto, H. Kurosu, S. Takakusagi, K. Asakura, H. Kondoh, Structural relationship between CoO_6 cluster and phosphate species in a cobaltphosphate water oxidation catalyst investigated by Co and P K-edge XAFS, Chem. Lett. 45 (2016) 277–279.